

A Novel Nonstationary 6G UAV-to-Ground Wireless Channel Model With 3-D Arbitrary Trajectory Changes

Hengtai Chang¹, Cheng-Xiang Wang¹, *Fellow, IEEE*, Yu Liu¹, Jie Huang¹, *Member, IEEE*, Jian Sun¹, *Member, IEEE*, Wensheng Zhang¹, *Member, IEEE*, and Xiqi Gao¹, *Fellow, IEEE*

Abstract—In order to provide reliable and efficient connections between unmanned aerial vehicles (UAVs) and ground stations (GSs), realistic UAV-to-ground channel models are indispensable. In this article, we propose a novel 3-D nonstationary geometry-based stochastic model (GBSM) for UAV-to-ground multiple-input–multiple-output (MIMO) channels. Distinctive UAV-to-ground channel characteristics, such as time-domain nonstationarity, distinctions between different altitudes, spatial consistency, and 3-D arbitrary UAV movement trajectories, are taken into account. By adjusting parameter settings, the proposed channel model framework is sufficiently general to support multiple frequency bands and multiple scenarios, including millimeter wave (mmWave) and massive MIMO configurations. Statistical properties, including power delay profile (PDP), stationary interval, space–time correlation function (STCF), and root-mean-square (RMS) delay spread are derived and analyzed for different frequencies and scenarios. The accuracy of the proposed model is validated by comparing its statistical properties with corresponding available channel measurements. The proposed channel model will provide a fundamental support for

the design, performance evaluation, and optimization of future UAV integrated sixth-generation (6G) wireless networks.

Index Terms—3-D nonstationary wireless channel models, arbitrary UAV trajectory, geometry-based stochastic model (GBSM), unmanned aerial vehicles (UAVs).

I. INTRODUCTION

THE RAPID development of unmanned aerial vehicles (UAVs) industry poses great challenges to UAV communication technologies. Many new applications of UAVs, such as aerial photography and remote sensing, not only demand reliable control and nonpayload communication links but also need high transmission data rate of payload links [1]. Utilizing future cellular networks to fulfill UAV communication demands is a feasible solution due to the extensive coverage and large bandwidth of current fifth-generation (5G) and future sixth-generation (6G) wireless communication networks [2]. According to the vision on potential applications of 6G wireless communication networks, UAVs will play more important roles in network coverage extension by serving as mobile base stations (BSs) [3], [4]. The deployment of aerial BSs has been regarded as a promising way to provide ubiquitous access from the sky toward the ground user equipment (UE) in specified areas and cases (e.g., hotspot areas, large public venues, and remote areas without network coverage) [5]. By combining UAVs with other key technologies related to satellite, terrestrial, and maritime communications, we can achieve Internet of Things (IoT) all over the world or global coverage through 6G space–air–ground–sea integrated networks [6], [7]. It is well known that a set of precise and easy-to-use channel models are critical for the design and performance optimization of communication systems [8]. Therefore, investigation of UAV channels has been a hot research topic recently.

Most previous investigations devoting to UAV-to-ground channel characterization can be categorized into two methods, i.e., measurement-based methods providing empirical channel models and simulation-based methods providing deterministic or stochastic channel models [9]. Through measurement-based methods, UAV-to-ground channel properties were investigated according to channel measurement data. For instance, a series of channel measurement campaigns were conducted in [10]–[12]. An S-C3B Viking aircraft was used to study the

Manuscript received April 16, 2020; revised July 24, 2020; accepted August 4, 2020. Date of publication August 21, 2020; date of current version June 7, 2021. This work was supported in part by the National Key Research and Development Program of China under Grant 2018YFB1801101; in part by the National Natural Science Foundation of China under Grant 6196206006 and Grant 61901109; in part by the Frontiers Science Center for Mobile Information Communication and Security; in part by the High-Level Innovation and Entrepreneurial Talent Introduction Program in Jiangsu; in part by the Research Fund of National Mobile Communications Research Laboratory, Southeast University, under Grant 2020B01; in part by the National Postdoctoral Program for Innovative Talents under Grant BX20180062; in part by the Fundamental Research Funds for the Central Universities under Grant 2242020R30001; in part by the Huawei Cooperation Project; in part by the EU H2020 RISE TESTBED2 Project under Grant 872172; in part by the Taishan Scholar Program of Shandong Province; in part by the Shandong Natural Science Foundation under Grant ZR2019BF040; and in part by the Fundamental Research Funds of Shandong University under Grant 2020GN032. (*Corresponding author: Cheng-Xiang Wang.*)

Hengtai Chang, Jian Sun, and Wensheng Zhang are with the Shandong Provincial Key Laboratory of Wireless Communication Technologies, School of Information Science and Engineering, Shandong University, Qingdao 266237, China (e-mail: hunter_chang@126.com; sunjian@sdu.edu.cn; zhangwsh@sdu.edu.cn).

Cheng-Xiang Wang, Jie Huang, and Xiqi Gao are with the National Mobile Communications Research Laboratory, School of Information Science and Engineering, Southeast University, Nanjing 210096, China, and also with the Pervasive Communication Research Center, Purple Mountain Laboratories, Nanjing 211111, China (e-mail: chxwang@seu.edu.cn; j_huang@seu.edu.cn; xqgao@seu.edu.cn).

Yu Liu is with the School of Microelectronics, Shandong University, Jinan 250101, China (e-mail: yuliu@sdu.edu.cn).

Digital Object Identifier 10.1109/JIOT.2020.3018479

air-to-ground channel characteristics at L-band and C-band in diverse environments. In [13], the channel between airship and ground station (GS) was measured at 2.5-GHz band, and comparison results showed that the air-to-ground channels are kind of special links with properties between terrestrial channels and land mobile satellite (LMS) channels. In [14], the UAV-to-ground channel was measured in a suburban scenario by exploiting cell-specific signals in long term evolution (LTE) networks. Statistical properties, such as path loss, shadowing, root-mean-square (RMS) delay spread (DS), were analyzed. Although channel measurements are the most intuitive methods to study wireless channels, it is too expensive and time-consuming to conduct channel measurement campaigns, especially in some extreme scenarios such as the UAV-to-ground scenario.

As for the simulation-based methods, they are able to provide channel simulation results based on electromagnetic wave propagation theory. Simulation-based methods can be divided into deterministic modeling methods and stochastic modeling methods. A typical deterministic modeling method is ray tracing, which can depict the realistic behavior of the electromagnetic wave propagation. Feng *et al.* [15] used ray tracing to evaluate the UAV-to-ground link coverage range in an urban scenario. In [16], a UAV-to-ground large-scale fading model supporting millimeter wave (mmWave) band was developed based on ray tracing simulation. The accuracy of deterministic modeling methods depends on the description of environmental layout including the terrain topography and the electromagnetic parameters of obstruction materials. Besides, the simulation of time-variant channels using deterministic methods will cause considerable computation complexity, which will decrease simulation efficiency [17].

In stochastic modeling methods, part of stochastic channel models were developed by modeling channel fading statistics as stochastic processes. In [12], wideband stochastic channel models were proposed based on the time delay line (TDL) structure from the measurement data. With explicit geometry relationships between transmitter (Tx), receiver (Rx), and scatterers, geometry-based stochastic models (GBSMs) are suitable for simulation of high-mobility communication channels, such as vehicle-to-vehicle (V2V) [18]–[20] and high speed train (HST) channels [21]–[25]. Similarly, UAV-to-ground channels can be modeled in the 3-D space by GBSM. Zeng *et al.* [26], [28] and Li and Cheng [27] used cylinder to describe the scatterers around the GSs. Statistical properties like temporal autocorrelation functions (ACFs) and spatial cross-correlation functions (CCFs) were derived according to geometry relationships. Chang *et al.* [29] and Jiang *et al.* [30] utilized the ellipsoid model to describe the wideband properties of UAV-to-ground multiple-input-multiple-output (MIMO) channels. However, these GBSMs ideally assume that scatterers are distributed on regular shaped cylinders, ellipsoids, or spheres, which cannot represent the realistic scenarios. In addition, 3-D UAV trajectories and spatial consistency are not taken into account in current GBSMs.

Besides, some standard UAV-to-ground channel models were proposed, such as the 3rd generation partnership project

(3GPP) model in technical report “Study on Enhanced LTE Support for Aerial Vehicles” [2]. Some channel parameters were provided, including path loss, Ricean K factor, angular distribution, etc. The distinctions between UAV-to-ground channel and terrestrial channel are parametrized, e.g., UAV heights were introduced to describe the channel parameters.

It is well known that a complete and useful channel model should be able to represent corresponding channel characteristics. UAV-to-ground channels present some unique channel properties due to changeable UAV trajectories in the 3-D space and time-varying properties introduced by UAV movement. These distinctive channel properties include but not limited to the following.

- 1) Arbitrary 3-D UAV trajectories and velocities will introduce the Doppler frequency shift and fast time-variant channel characteristics.
- 2) UAVs are usually fly in low altitudes, e.g., below 150 m or 100 m, where channel characteristics are highly dependent on UAV altitudes.
- 3) UAV movements cause the continuous changing of channel scenarios and bring the nonstationary and spatial consistency channel properties.

Precise characterization of UAV-to-ground channels is the foundation of follow-up technical research. For instance, Quality of Service (QoS)-aware UAV trajectory optimization needs channel fading information along the 3-D UAV trajectory. Strategy selections in UAV-aided cooperation and relay techniques largely depend on heterogeneous channel conditions in different scenarios and altitudes. However, existing UAV-to-ground channel models have their limitations to accurately describe such channel characteristics. To the best of our knowledge, the UAV-to-ground channel model supporting arbitrary UAV trajectory and spatial consistency in 3-D space is still missing. Long time channel simulation considering time-varying of channel statistical properties according to UAV height is also rarely investigated.

Motivated by the above background and gaps of current research, a novel nonstationary GBSM for UAV-to-ground channels is proposed in this article. The contributions and novelties of this article include the following.

- 1) The proposed model supports the channel generation through arbitrary 3-D trajectories and velocities. Considering the acceleration and deceleration of UAVs, adaptive track sampling is used to enhance simulation efficiency.
- 2) To ensure the spatial consistency of channel properties, a grid-based correlated large-scale parameter (LSP) generation method is applied. Considering the different statistical property distributions at different UAV altitudes, the grids are divided into multiple layers according to altitudes with different parameter distributions.
- 3) Time-variant small-scale parameters (SSPs) and cluster evolution process are introduced in time and array domain to mimic the nonstationarity. High resolutions of SSPs in time and space domains enable the proposed model to support mmWave bands and massive MIMO configuration.

4) Statistical properties of the proposed UAV-to-ground channel model are derived, including power delay profile (PDP), space-time correlation function (STCF), stationary interval, RMS Doppler spread, etc. The simulation results are validated by channel measurement results.

The remainder of this article is organized as follows. In Section II, the proposed channel model is illustrated in detail, including geometry construction and LSP/SSP generation processes. Statistical properties, such as PDP, STCF, stationary interval, RMS Doppler spread, and RMS DS, are derived in Section III. In Section IV, channel simulation results are analyzed. Finally, conclusions and future works are given in Section V.

II. THREE-DIMENSIONAL WIDEBAND UAV-TO-GROUND MIMO GBSM

The channel between UAV and GS is affected by large-scale fading and small-scale fading. A widely used representation form of fading channels is the channel impulse response (CIR), and a complete MIMO CIR matrix is given by

$$\mathbf{H} = [\text{PL} \cdot \text{SH}]^{1/2} \cdot \mathbf{H}_s \quad (1)$$

where PL denotes the path loss caused by propagation distance between the UAV and GS. 3GPP gives a complete UAV-to-ground path loss model at multifrequencies and in multisenarios [2]. Shadowing is represented by SH and considered as an LSP, which will be discussed later. The matrix \mathbf{H}_s denotes small-scale fading of different antenna pairs.

Small-scale channel fading is caused by multipath components (MPCs) generated by terrains and buildings near the ground. Fig. 1(a) gives a typical scenario of UAV-to-ground channel including all possible MPC types. The transmitted signal can arrive by Line-of-Sight (LoS) path, single bounce, and multibounce. In order to simulate the UAV-to-ground channel more accurately and reduce unnecessary computation complexity, we construct the UAV-to-ground channel using geometry shapes to effectively abstract real-world scatterers.

A typical 3-D MIMO channel between UAV with n_T antenna elements and GS with n_R antenna elements is presented in Fig. 1(b). Both UAV and GS are equipped with uniform linear arrays (ULAs). The UAV is set as Tx and the GS is set as Rx. To simplify description, only the n th ($n = 1, \dots, N_{pq}(t)$) path is illustrated in detail, in which $N_{pq}(t)$ is the total path number in the link between Tx and Rx at the time instant t . Considering for massive MIMO antenna configuration, the observable cluster set can be different for different antenna pairs. Only clusters observable for both Tx and Rx antenna elements will be considered in channel simulation. For instance, in Fig. 1(b), $n + 1$ th path will be ignored in channel simulation. Meanwhile, the first and last bounce clusters are specified as spheres containing yellow dots, i.e., the cluster beside Tx, C_n^A , and the cluster beside Rx, C_n^Z . The propagation path between C_n^A and C_n^Z is abstracted as a virtual link with a given delay. Note that for single bounce rays, C_n^A and C_n^Z are regarded as the same cluster and the delay of virtual link is set to zero. In this channel modeling framework, Tx, Rx, C_n^A , C_n^Z all can be moving, i.e., changing coordinates

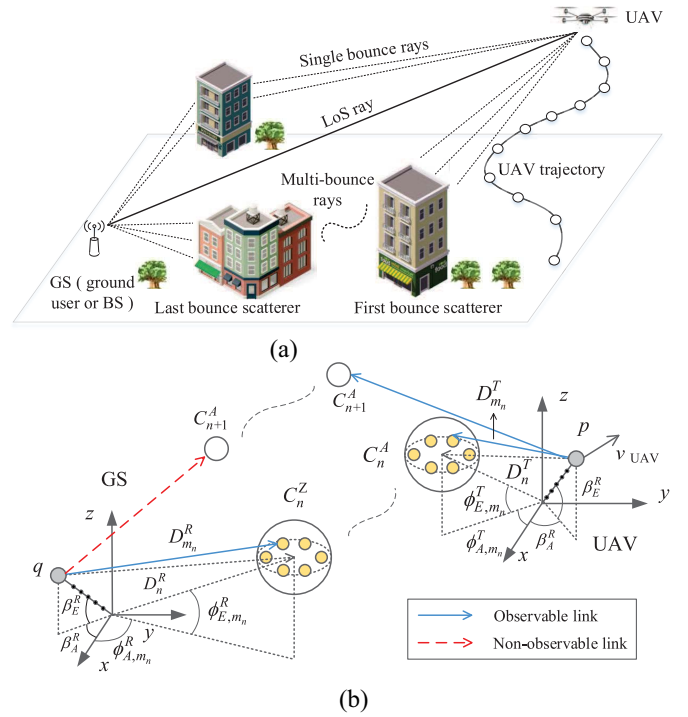


Fig. 1. Typical UAV-to-ground communication scenario. Scatterers like buildings are abstracted as scattering clusters. (a) Real world scene. (b) Abstract scene.

\mathbf{A}_0^T , \mathbf{A}_0^R , C_n^A , and C_n^Z with respect to (w.r.t.) time. In case of UAV to fixed BS channel simulation, BS can be regarded as static. The Azimuth Angle of Departure (AAoD) and Elevation Angle of Departure (EAoD) of the m th ray in cluster C_n^A transmitted from Tx are denoted by ϕ_{A,m_n}^T and ϕ_{E,m_n}^T , respectively. Azimuth Angle of Arrival (AAoA) and Elevation Angle of Arrival (EAoA) of the m th ray in cluster C_n^Z received from Rx are denoted by ϕ_{A,m_n}^R and ϕ_{E,m_n}^R . Similarly, the EAoD, EAoA, AAoD, and AAoA of the LoS path are denoted by $\phi_{A,LoS}^T$, $\phi_{E,LoS}^T$, $\phi_{A,LoS}^R$, and $\phi_{E,LoS}^R$, respectively. For clarity, the key parameters involved in channel modeling are listed in Table I.

The small-scale fading of MIMO channel with given setting can be represented by a matrix $\mathbf{H}_s = [h_{pq}(t, \tau)]_{n_T \times n_R}$. The complex CIR of MIMO fading channel between the p th Tx antenna element and the q th Rx antenna element can be represented by the superposition of the LoS and non-LoS (NLoS) components, i.e.,

$$h_{pq}(t, \tau) = \sqrt{\frac{K_R}{K_R + 1}} h_{pq}^{\text{LoS}}(t, \tau) + \sqrt{\frac{1}{K_R + 1}} h_{pq}^{\text{NLoS}}(t, \tau) \quad (2)$$

where K_R is the K-factor (KF). The NLoS components $h_{pq}^{\text{NLoS}}(t, \tau)$ can be expressed as

$$h_{pq}^{\text{NLoS}}(t, \tau) = \sum_{n=1}^{N_{pq}(t)} \sum_{m=1}^{M_n} \left[\begin{array}{c} F_{q,V} \left(\phi_{E,m_n}^R, \phi_{A,m_n}^R \right) \\ F_{q,H} \left(\phi_{E,m_n}^R, \phi_{A,m_n}^R \right) \end{array} \right]^T \times \left[\begin{array}{cc} e^{j\theta_{mn}^{VV}} & \sqrt{\kappa_{mn}^{-1}} e^{j\theta_{mn}^{VH}} \\ \sqrt{\kappa_{mn}^{-1}} e^{j\theta_{mn}^{HV}} & e^{j\theta_{mn}^{HH}} \end{array} \right]$$

TABLE I
DEFINITION OF SIGNIFICANT CHANNEL MODEL PARAMETERS

Symbol	Definition
$\mathbf{A}_0^T / \mathbf{A}_0^R$	Coordinates of first Tx/Rx antenna elements
$\mathbf{C}_n^A / \mathbf{C}_n^Z$	Coordinates of center of clusters C_n^A / C_n^Z
$\mathbf{C}_{m_n}^A / \mathbf{C}_{m_n}^Z$	Coordinates of scattering points of m -th ray in the cluster C_n^A / C_n^Z
β_A^T / β_A^R	Azimuth angles of the Tx/Rx antenna array
β_E^T / β_E^R	Elevation angles of the Tx/Rx antenna array
δ_T / δ_R	Antenna spacings of the Tx and Rx arrays
$\phi_{A,m_n}^T / \phi_{E,m_n}^T$	AAoD and EAoD of the m th ray in the n th path
$\phi_{A,m_n}^R / \phi_{E,m_n}^R$	AAoA and EAoA of the m th ray in the n th path
$\phi_{A,LoS}^T / \phi_{E,LoS}^T$	AAoD and EAoD of the LoS component
$\phi_{A,LoS}^R / \phi_{E,LoS}^R$	AAoA and EAoA of the LoS component
$\theta_{A,n}^A / \theta_{E,n}^A$	Azimuth/elevation angles of the cluster C_n^A velocity
$\theta_{A,n}^Z / \theta_{E,n}^Z$	Azimuth/elevation angles of the cluster C_n^Z velocity
D_n^T / D_n^R	Distances between Tx/Rx and C_n^A / C_n^Z
λ_G / λ_R	Generation rate and recombination rate of clusters
$D_{m_n}^R / D_{m_n}^T$	Lengths from Tx/Rx to C_n^A / C_n^Z via m th ray
$N_{pq}(t)$	Time-variant clusters number
M_n	Rays number in the n th path

$$\begin{aligned} & \times \begin{bmatrix} F_{p,V}(\phi_{E,m_n}^T, \phi_{A,m_n}^T) \\ F_{p,H}(\phi_{E,m_n}^T, \phi_{A,m_n}^T) \end{bmatrix} \sqrt{P_{pq,m_n}(t)} \\ & \times e^{j2\pi f_c \tau_{pq,m_n}(t)} \cdot \delta(\tau - \tau_{pq,m_n}(t)) \end{aligned} \quad (3)$$

where $\{\cdot\}^T$ denotes the transposition operation, f_c is the carrier frequency, and $F_{p/q,V}$ and $F_{p/q,H}$ are the antenna patterns of Tx/Rx for vertical and horizontal polarizations, respectively. Besides, κ_{m_n} is the cross polarization power ratio, $\theta_{m_n}^{VV}$, $\theta_{m_n}^{VH}$, $\theta_{m_n}^{HV}$, and $\theta_{m_n}^{HH}$ are initial phases subject to uniform distribution in $(0, 2\pi]$, $P_{pq,m_n}(t)$ and $\tau_{pq,m_n}(t)$ are the powers and delays of the m th ray in the n th cluster between Tx antenna and Rx antenna at time t , respectively. For the LoS component, it can be expressed as

$$\begin{aligned} h_{pq}^{\text{LoS}}(t, \tau) &= \begin{bmatrix} F_{q,V}(\phi_{E,LoS}^R, \phi_{A,LoS}^R) \\ F_{q,H}(\phi_{E,LoS}^R, \phi_{A,LoS}^R) \end{bmatrix}^T \begin{bmatrix} e^{j\theta_{LoS}^{VV}} & 0 \\ 0 & e^{j\theta_{LoS}^{HH}} \end{bmatrix} \\ & \times \begin{bmatrix} F_{p,V}(\phi_{E,LoS}^T, \phi_{A,LoS}^T) \\ F_{p,H}(\phi_{E,LoS}^T, \phi_{A,LoS}^T) \end{bmatrix} \\ & \times e^{j2\pi f_c \tau_{pq,LoS}(t)} \delta(\tau - \tau_{pq,LoS}(t)) \end{aligned} \quad (4)$$

where θ_{LoS}^{VV} and θ_{LoS}^{HH} are random phases in $(0, 2\pi]$, and $\tau_{pq,LoS}$ is the time delay of LoS path.

Due to the movement of UAV, the environment will present changes w.r.t. time axis, i.e., nonstationary properties in time domain. In order to capture these changes accurately, the cluster evolution algorithm is applied to obtain time-variant channel coefficients. To be specific, channel simulation parameters can be divided into two types: 1) LSPs, including DS, Rician KF, shadow fading (SF), and angular spread (AS)

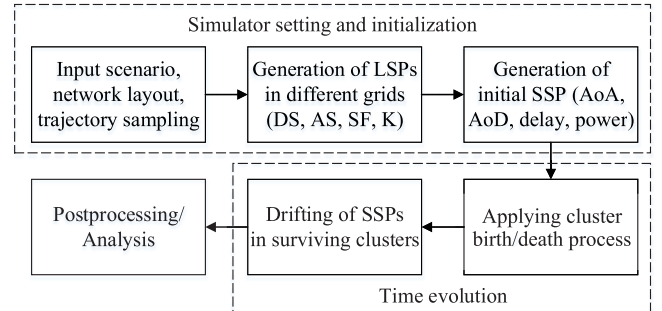


Fig. 2. Flow chart of channel simulation process.

which change slowly and remain constant within a certain area and 2) SSFs, including AoA, AoD, delay, and power of each cluster generated or updated for each track segment. The specific flow chart is shown in Fig. 2.

Before channel generation, the UAV trajectory will be divided into several small trajectory segments, and within each segment the channel can be seen as constant. Therefore, the UAV-to-ground channel with given trajectory can be described by a series of channel snapshots for different locations like Fig. 1(a) shown. In order to capture fast variant channel properties, proper trajectory sample methods should be applied. In time domain, the trajectory can be divided by temporal sampling according to sampling theorem [31]

$$f_T \geq 4 \cdot \max |f_{\max}| \geq 4 \cdot \frac{\max |v_{\text{UAV}}| + |v_g| + |v_c|}{\lambda} \quad (5)$$

where f_T is the sampling number per second, f_{\max} is the maximum Doppler frequency value, $|v_{\text{UAV}}|$ and $|v_g|$ are absolute values of UAV and GS velocities, and $|v_c|$ denotes the

velocity summation of moving scatterers C_n^A and C_n^Z with $|v_c| = |v_A| + |v_Z|$. Equation (5) specifies the lower bound for time sampling rate. In temporal sampling, the distance between adjacent segments will vary w.r.t. UAV velocity, i.e., $\delta_d = v_{\text{UAV}}/f_T$. In space domain, the trajectory can be divided w.r.t. distance along the trajectory according to corresponding spatial sampling theorem, and the lower bound of spatial sampling is determined by minimum UAV velocity along the trajectory

$$f_S \geq 4 \cdot \frac{\min|v_{\text{UAV}}| + |v_g| + |v_c|}{\lambda \cdot \min|v_{\text{UAV}}|} \quad (6)$$

where f_S is the sampling number per meter along the UAV trajectory, and the sample interval along the trajectory is $\delta_d = 1/f_S$. The temporal sampling and spatial sampling can transform to each other by resampling. Note that when GS and scatterers in the scenario are static, i.e., $|v_g| = |v_c| = 0$ m/s, the spatial sampling rate will reduce to $f_S = 4/\lambda$, which agrees with the result in [31].

For channel simulation of arbitrary 3-D UAV trajectories, the spatial sampling method that fulfills one condition and has fewer sampling points along the same UAV trajectory is recommended first for efficiency. The condition is described as

$$\frac{\max|v_{\text{UAV}}|}{\bar{v}_{\text{UAV}}} - 1 > \frac{|v_g| + |v_c|}{\min|v_{\text{UAV}}|} - \frac{|v_g| + |v_c|}{|\bar{v}_{\text{UAV}}|} \quad (7)$$

where \bar{v}_{UAV} is the mean value of UAV velocity along the trajectory.

There are three significant mechanisms modeling nonstationary properties caused by movement of the UAV, i.e., the grid-based LSPs generation, cluster birth–death process, and the drifting of SSPs. We will introduce these three mechanisms below.

A. Grid-Based LSPs Generation

Positions and parameters of scattering clusters are dependent on LSPs. Therefore, LSPs in the UAV flight space should be generated and saved before cluster time evolution. In channel generation, in each segment, only LSPs in the segment corresponding grid are used for cluster generation. Considering the spatial consistency of LSPs, i.e., the fact that adjacent segments in the UAV trajectory may share similar LSPs, the UAV flight space is first divided into several layers with certain height Δh at different altitudes. Then, each layer is divided into multiple grids with size of $D_g \times D_g$, and LSPs in each grid are spatial consistent. The LSP matrices in top layer and bottom layer, i.e., $\tilde{\mathbf{r}}_{h_t}$ and $\tilde{\mathbf{r}}_{h_b}$, are generated first according to the available parameter sets. For carrier frequency bands below 6 GHz, the parameter set from 3GPP TR 36.777 [2] and some available measurement data [9], [11]–[14] are recommended. As for higher frequency bands, e.g., mmWave bands, since there are no complete available UAV-to-ground channel measurement data, up to date terrestrial channel models supporting mmWave such as, 3GPP TR 38.901 [32] and 5GCM [33], can be applied. Considering the correlation of LSPs between adjacent grids, an exponential spatial filter is used to correlate independent LSPs in top layer and bottom

layer LSP matrices [34]

$$\tilde{r}_{u,w} = \sum_{x=0}^U \sum_{y=0}^W r_{x,y} \cdot F(u-x, w-y) \quad (8)$$

where $\tilde{r}_{u,w}$ and $r_{x,y}$ are correlated and independent LSPs at grids (u, w) and (x, y) in top or bottom layer, $U \times W$ denotes total grids number, and $F(u-x, w-y)$ is the exponential filter defined by

$$F(u-x, w-y) = \exp\left(-\frac{D_g \cdot \|u-x, w-y\|}{D_c^S}\right) \quad (9)$$

where D_c^S is the scenario-dependent correlation factor in time domain with typical values of 10 m, 30 m, 50 m, 100 m, and D_g usually with typical value of 1 m [35]. Considering the correlation between different altitudes at the same grid location, the LSPs of middle layers are calculated according to the altitude differences from current layer to top layer and bottom layer

$$\tilde{\mathbf{r}}_h = \tilde{\mathbf{r}}_{h_t} \cdot \frac{h-h_b}{h_t-h_b} + \tilde{\mathbf{r}}_{h_b} \cdot \frac{h_t-h}{h_t-h_b}, \quad h_b < h < h_t \quad (10)$$

where $\tilde{\mathbf{r}}_h$ is the LSP matrix at corresponding altitude h , $\tilde{\mathbf{r}}_{h_t}$ and $\tilde{\mathbf{r}}_{h_b}$ are LSP matrices at top layer and bottom layer with corresponding altitudes h_t and h_b , respectively. It is worth mentioning that the LSPs vary w.r.t. change of grid and layer, while LSPs in the same layer same grid are consistent.

Taking generation of Ricean K factor in dB for instance in Fig. 3, independent K factors in top layer and bottom layer are generated first according to the Gaussian process with corresponding mean value μ_{K_R} and standard deviation σ_{K_R} . These two parameters are defined in 3GPP TR 36.777 [2, Table B.1.2-1] as

$$\mu_{K_R} = 22.55 \log_{10}(h_{\text{UT}}) - 4.72 \quad (11)$$

$$\sigma_{K_R} = 6.988 \exp(0.01659 h_{\text{UT}}) \quad (12)$$

where h_{UT} is the UAV altitude. Here, we substitute $h_{\text{UT}} = h_t$ and $h_{\text{UT}} = h_b$ to get μ_{K_R} and σ_{K_R} at top layer and bottom layer. Then correlated K factors in top layer and bottom layer are obtained by spatial filtering. It can be seen that after spatial filtering, the continuous spatial variation of K factor is realized. Finally, multilayer K factors are calculated according to K factors in top/bottom layers and altitudes of middle layers. Since UAVs usually carry out complex operations, such as rising, diving, hovering, acceleration, and deceleration in 3-D space, in the choice of the LSPs at each segment, it first checks which grid the UAV locates and then assigns the corresponding LSPs in calculation of SSPs.

B. Time-Array Cluster Birth-Death Process

Since the movement of UAVs, scattering cluster existing in the last segment may disappear in the next segment, and the new clusters also can appear in any segments, which can be described as birth/death process. This process also will happen in antenna array domain, i.e., the cluster observable for one antenna element may be unobservable for another antenna element. There are two parameters controlling the birth/death process, i.e., the generation rate of clusters λ_G and

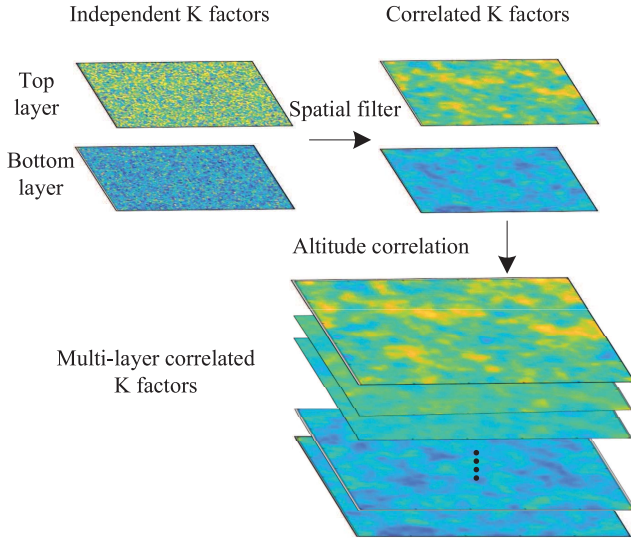


Fig. 3. Generation process of multilayer correlated K factor.

the recombination rate of clusters λ_R . The survival probability $P_s^T(\delta_d, \Delta d_T)$ of a cluster surviving over the trajectory segment δ_d and Tx antenna element spacing Δd_T is computed as

$$P_s^T(\delta_d, \Delta d_T) = \exp\left[-\lambda_R \left(\frac{\delta_d}{D_c^S} + \frac{\Delta d_T}{D_c^A}\right)\right] \quad (13)$$

where D_c^A is the scenario-dependent correlation factor in array domain. At the Rx side, the survival probability $P_s^R(\delta_d, \Delta d_R)$ of a cluster surviving over the trajectory segment δ_d and Rx antenna element spacing Δd_R can be computed similarly. Since each antenna element has its own observable cluster set, a cluster can contribute to the received power only if can be seen by at least one transmit antenna element and one receive antenna element. Therefore, the joint survival probability of a cluster is expressed as

$$P_s(\delta_d, \Delta d_T, \Delta d_R) = P_s^T(\delta_d, \Delta d_T) \cdot P_s^R(\delta_d, \Delta d_R). \quad (14)$$

Meanwhile, a random number of new clusters will be generated in the now segment or antenna pair according to the Poisson process. The mean value of new generated clusters can be calculated as

$$\mathbb{E}(N_{\text{new}}) = \frac{\lambda_G}{\lambda_R} (1 - P_s(\delta_d, \Delta d_T, \Delta d_R)). \quad (15)$$

For each new generated cluster, the 3-D coordinate is generated according to LSPs in the corresponding grid. The position of a cluster is determined by three parameters, i.e., azimuth angle (AAoA, AAoD), elevation angle (EAoA, EAoD), and distance. For instance, the AAoA and AAoD of cluster C_n^Z can be calculated as

$$\phi_{A,n}^R = \text{AS}[\phi_{A,n}^R] Y_{A,n}^R + \psi_{A,n}^R \quad (16)$$

$$\phi_{E,n}^R = \text{AS}[\phi_{E,n}^R] Y_{E,n}^R + \psi_{E,n}^R \quad (17)$$

where $Y_{A,n}^R$ and $Y_{E,n}^R$ follow normal distribution $\mathcal{N}(0, 1)$, $\text{AS}[\phi_{A,n}^R]$ and $\text{AS}[\phi_{E,n}^R]$ are ASs, and $\psi_{A,n}^R$ and $\psi_{E,n}^R$ are mean values of AAoA and EAoA. The distances from Rx to C_n^Z , D_n^R , is defined as a non-negative variable in accordance with exponential distribution. Then, same generation process is applied

to parameters of C_n^A , and the positions of scattering clusters C_n^A and C_n^Z are calculated, respectively, by

$${}^{[0]}\mathbf{C}_n^A = {}^{[0]}\mathbf{A}_0^T + D_n^T \cdot \begin{bmatrix} \cos \phi_{A,n}^T \cdot \cos \phi_{E,n}^T \\ \sin \phi_{A,n}^T \cdot \cos \phi_{E,n}^T \\ \sin \phi_{E,n}^T \end{bmatrix}^T \quad (18)$$

$${}^{[0]}\mathbf{C}_n^Z = {}^{[0]}\mathbf{A}_0^R + D_n^R \cdot \begin{bmatrix} \cos \phi_{A,n}^R \cdot \cos \phi_{E,n}^R \\ \sin \phi_{A,n}^R \cdot \cos \phi_{E,n}^R \\ \sin \phi_{E,n}^R \end{bmatrix}^T \quad (19)$$

where superscript ${}^{[0]}\{\cdot\}$ denotes coordinate while clusters C_n^A and C_n^Z is generating. Finally, because of the spread of the scattering cluster in space, the coordinate of m th ray in $C_n^{A/Z}$ can be obtained by

$${}^{[0]}\mathbf{C}_{m_n}^{A/Z} = {}^{[0]}\mathbf{C}_n^{A/Z} + \begin{bmatrix} \Delta x_{m_n}^{A/Z} & \Delta y_{m_n}^{A/Z} & \Delta z_{m_n}^{A/Z} \end{bmatrix} \quad (20)$$

where $[\Delta x_{m_n}^{A/Z} \ \Delta y_{m_n}^{A/Z} \ \Delta z_{m_n}^{A/Z}]$ can be modeled as 3-D Gaussian distribution. The 3-D Gaussian scattering assumption is widely used because it has been observed experimentally in channel measurement [36]. The probability density function of 3-D Gaussian distribution with given standard deviation σ_n [37] can be written as

$$P\left(\Delta x_{m_n}^{A/Z}, \Delta y_{m_n}^{A/Z}, \Delta z_{m_n}^{A/Z}\right) = \frac{\exp\left(-\left(\Delta x_{m_n}^{A/Z} + \Delta y_{m_n}^{A/Z} + \Delta z_{m_n}^{A/Z}\right)/2\sigma_n^2\right)}{2\pi^{3/2}\sigma_n^3}. \quad (21)$$

C. Updating Drifting SSPs

After generation of cluster positions, SSPs will be calculated according to geometry relationships between transceivers and clusters in each segment. For the trajectory segment at time instant t , the coordinates of scattering clusters C_n^A and C_n^Z are

$$\mathbf{C}_{m_n}^A = {}^{[0]}\mathbf{C}_{m_n}^A + v_A(t - t_n^b) \cdot \begin{bmatrix} \cos \theta_{A,n}^A \cdot \cos \theta_{E,n}^A \\ \sin \theta_{A,n}^A \cdot \cos \theta_{E,n}^A \\ \sin \theta_{E,n}^A \end{bmatrix}^T$$

$$\mathbf{C}_{m_n}^Z = {}^{[0]}\mathbf{C}_{m_n}^Z + v_Z(t - t_n^b) \cdot \begin{bmatrix} \cos \theta_{A,n}^Z \cdot \cos \theta_{E,n}^Z \\ \sin \theta_{A,n}^Z \cdot \cos \theta_{E,n}^Z \\ \sin \theta_{E,n}^Z \end{bmatrix}^T \quad (22)$$

where t_n^b is the birth time of clusters C_n^A and C_n^Z . Besides, $\theta_{A,n}^A$, $\theta_{E,n}^A$, $\theta_{A,n}^Z$, and $\theta_{E,n}^Z$ are azimuth and elevation angles of clusters C_n^A and C_n^Z velocities.

The emergent vector from p th Tx antenna element to C_n^A via m th ray, and incidence vector from cluster C_n^Z to q th Rx antenna element via m th ray can be obtained by

$$\mathbf{r}_{m_n}^T = \mathbf{C}_{m_n}^A - \mathbf{A}_p^T \quad (23)$$

$$\mathbf{r}_{m_n}^R = \mathbf{A}_q^R - \mathbf{C}_{m_n}^Z \quad (24)$$

where \mathbf{A}_p^T and \mathbf{A}_q^R denote coordinates of p th Tx antenna element and q th Rx antenna element which can be expressed by

$$\mathbf{A}_p^T = \mathbf{A}_0^T + (p-1) \cdot \delta_T \cdot \begin{bmatrix} \cos \beta_A^T \cdot \cos \beta_E^T \\ \sin \beta_A^T \cdot \cos \beta_E^T \\ \sin \beta_E^T \end{bmatrix}^T \quad (25)$$

TABLE II
 GENERATION OF SIGNIFICANT CHANNEL MODEL PARAMETERS

Parameters	Distribution	Generation methods
σ_τ	Exponential	Randomly generated according to channel measurement
σ_n	Gaussian	Generated by fitting measurement data [14]
$\phi_{A,n}^T, \phi_{E,n}^T, \phi_{A,n}^R, \phi_{E,n}^R$	Wrapped Gaussian	Randomly generated according to 3GPP TR 36.777
D_n^T, D_n^R	Exponential	Generated by fitting measurement data [14]
M_n	Poisson	Determined by assumption

$$\mathbf{A}_q^R = \mathbf{A}_0^R + (q-1) \cdot \delta_R \cdot \begin{bmatrix} \cos \beta_A^R \cdot \cos \beta_E^R \\ \sin \beta_A^R \cdot \cos \beta_E^R \\ \sin \beta_E^R \end{bmatrix}^T. \quad (26)$$

Based on the emergent and incidence vectors, the AoDs and AoAs of n th path can be expressed as

$$\phi_{A,m_n}^X = \arctan_2(r_{m_n,y}^X, r_{m_n,x}^X) \quad (27)$$

$$\phi_{E,m_n}^X = \arcsin(r_{m_n,z}^X, D_{m_n}^X) \quad (28)$$

where $\arctan_2(\cdot)$ is the four-quadrant inverse tangent operation, $r_{m_n,y}^X$, $r_{m_n,x}^X$, and $r_{m_n,z}^X$ are x , y , and z components of the vector $\mathbf{r}_{m_n}^X$, in which $X = \{T, R\}$. Note that the subscripts p/q are omitted for clarity. Besides, the distance of m th ray from scattering cluster C_n^A to p th Tx antenna element and the distance of m th ray from scattering cluster C_n^Z to q th Rx antenna element are expressed by $D_{m_n}^X = \{D_{p,m_n}^T, D_{q,m_n}^R\}$, with $D_{p,m_n}^T = \|\mathbf{r}_{m_n}^T\|$ and $D_{q,m_n}^R = \|\mathbf{r}_{m_n}^R\|$.

Meanwhile, the AoA and AoD of LoS component can be obtained by the vector of LoS path

$$\mathbf{r}_{pq}^{\text{LoS}} = \mathbf{A}_p^R - \mathbf{A}_q^T. \quad (29)$$

Similar to NLoS computation

$$\phi_A^{\text{LoS}} = \arctan_2(r_{pq,y}^{\text{LoS}}, r_{pq,x}^{\text{LoS}}) \quad (30)$$

$$\phi_E^{\text{LoS}} = \arcsin(r_{pq,z}^{\text{LoS}}, D_{pq}^{\text{LoS}}) \quad (31)$$

where $r_{pq,x}^{\text{LoS}}$, $r_{pq,y}^{\text{LoS}}$, and $r_{pq,z}^{\text{LoS}}$ denote x , y , and z components of $\mathbf{r}_{pq}^{\text{LoS}}$, and the length of LoS path from p th Tx antenna element to q th Rx antenna element is expressed as $D_{pq}^{\text{LoS}} = \|\mathbf{r}_{pq}^{\text{LoS}}\|$.

The delays and powers of different paths are dependent on the total propagation distance of paths. For the m th ray in n th path, the total propagation delay is

$$\tau_{pq,m_n}(t) = (D_{p,m_n}^T + D_{q,m_n}^R)/c + \tilde{\tau}_{m_n} \quad (32)$$

where $\tilde{\tau}_{m_n}$ is the time delay caused by propagation distance of virtual link between $C_{m_n}^A$ and $C_{m_n}^Z$ and is modeled as $\tilde{\tau}_{m_n} = \tilde{d}_{m_n}/c + \tau_{C,\text{link}}$ where \tilde{d}_{m_n} is distance between $C_{m_n}^A$ and $C_{m_n}^Z$, and $\tau_{C,\text{link}}$ is a non-negative variable which assumed to be exponentially distributed, and can be expressed by

$$\tau_{C,\text{link}} = -r_\tau \sigma_\tau \cdot \ln u_n \quad (33)$$

where u_n is uniformly distributed within $(0, 1)$, r_τ is the delay scalar, and σ_τ is the DS [40]. Note that ray delays are calculated at each segment, the phase shift caused by the Doppler effect is also included in CIR generation process. Based on

the time-variant ray delays, the ray powers can be generated according to single slope exponential distribution

$$P'_{pq,m_n}(t) = \left[\exp\left(-\tau_{pq,m_n}(t) \frac{r_\tau - 1}{r_\tau \sigma_\tau}\right) 10^{-\frac{Y_n}{10}} \right] \quad (34)$$

where Y_n is the per cluster shadowing in dB. Finally, the ray powers are normalized to 1, and the final powers are

$$P_{pq,m_n}(t) = P'_{pq,m_n}(t) / \sum_{n=1}^{N_{pq}(t)} \sum_{m_n=1}^{M_n} P'_{pq,m_n}(t). \quad (35)$$

For clarity, some generation methods of significant parameters are also listed in Table II. It is worth mentioning that, based on the more practical near field spherical wave propagation than plane wave propagation, SSPs for different antenna pairs are generated, respectively, according to geometry relation between antenna elements and scatterer, which will increase the spatial resolution of the proposed model. Higher space resolution enables channel simulation with increasing antenna size.

III. STATISTICAL PROPERTIES OF PROPOSED MODEL

A. Time-Variant PDP

The time-variant PDP $\Lambda_{pq}(t, \tau)$ directly reveal the power and delay of MPCs, and it can be expressed as

$$\Lambda_{pq}(t, \tau) = \sum_{n=1}^{N_{pq}(t)} \sum_{m_n=1}^{M_n} P_{pq,m_n}(t) \delta(\tau - \tau_{m_n}(t)). \quad (36)$$

The variation of PDP is caused by evolutions of clusters. Different UAV trajectories or velocities will lead to different PDP variation trends.

B. Stationary Interval

The stationary interval is a statistical property defined as the maximum duration within which the channel can be seen as stationary. For UAV communication systems, the channel estimation frequency can be determined by the value of stationary interval.

Here, method of local region of stationary (LRS) is used to calculate the stationary interval [39]. First, the correlation coefficient between two PDPs in t and $t + \Delta t$ is obtained by

$$c(t, \Delta t) = \frac{\int \Lambda_{pq}(t, \tau) \cdot \Lambda_{pq}(t + \Delta t, \tau) d\tau}{\max\left\{\int \Lambda_{pq}(t, \tau)^2 d\tau, \int \Lambda_{pq}(t + \Delta t, \tau)^2 d\tau\right\}}. \quad (37)$$

Then the stationary interval can be calculated as the largest interval within which the correlation coefficient beyond a certain threshold c_{thresh} , i.e.,

$$T_s(t) = \max\{\Delta t | c(t, \Delta t) \geq c_{\text{thresh}}\}. \quad (38)$$

In most current channel investigations, the correlation coefficient threshold is empirically set to 80% and this value can be adjusted according to specific requirements [8].

C. Time-Variant Transfer Function

The time-variant transfer function is defined as the Fourier transform of time-variant CIR $h_{pq}(t, \tau)$ w.r.t. time delay τ

$$H_{pq}(t, f) = \int_{-\infty}^{\infty} h_{pq}(t, \tau) e^{-j2\pi f \tau} d\tau. \quad (39)$$

Since the time delays are discrete defined for each ray in our proposed model, the integral operation can be simplified to summation operation, i.e.,

$$H_{pq}(t, f) = \sum_{n=1}^{N_{pq}(t)} \sum_{m_n=1}^{M_n} h_{pq, m_n}(t) e^{-j2\pi f \tau_{pq, m_n}(t)}. \quad (40)$$

In addition, the coherence bandwidth is obtained from calculation of correlation between different frequency bands. Usually, the 90% coherence bandwidth measures the bandwidth in which the channel can be regarded as flat [40].

D. Local STCF

The local STCF is defined as the correlation between $h_{pq}(t)$ and $h_{\tilde{p}\tilde{q}}(t - \Delta t)$

$$R_{pq, \tilde{p}\tilde{q}}(t, f; \Delta d, \Delta t) = \mathbb{E}\left\{h_{pq}(t) h_{\tilde{p}\tilde{q}}^*(t - \Delta t)\right\}. \quad (41)$$

Substituting (2) into (41), the local STCF can be obtained by superposition of LoS part and NLoS part

$$R_{pq, \tilde{p}\tilde{q}}(t, f; \Delta d, \Delta t) = \frac{K_R}{K_R + 1} R_{pq, \tilde{p}\tilde{q}}^{\text{LoS}}(t, f; \Delta d, \Delta t) + \frac{1}{K_R + 1} \times \sum_{n=1}^{N_{pq}(t)} R_{pq, \tilde{p}\tilde{q}, n}^{\text{NLoS}}(t, f; \Delta d, \Delta t). \quad (42)$$

For the local STCF of LoS part, it has the expression of

$$R_{pq, \tilde{p}\tilde{q}}^{\text{LoS}}(t, f; \Delta d, \Delta t) = \left[P_{pq}^{\text{LoS}}(t) P_{\tilde{p}\tilde{q}}^{\text{LoS}}(t - \Delta t) \right]^{\frac{1}{2}} \cdot e^{j\frac{2\pi}{\lambda} [d_{pq}^{\text{LoS}}(t) - d_{\tilde{p}\tilde{q}}^{\text{LoS}}(t - \Delta t)]} \quad (43)$$

where $\Delta d = \{\Delta d_T, \Delta d_R\}$ is the antenna elements spacing of Tx and Rx with $\Delta d_T = \delta_{\tilde{p}} - \delta_p$ and $\Delta d_R = \delta_{\tilde{q}} - \delta_q$. For the NLoS part, it can be expressed as

$$R_{pq, \tilde{p}\tilde{q}, n}^{\text{NLoS}}(t, f; \Delta d, \Delta t) = P_s(t, \Delta t, \Delta d) \cdot \mathbb{E} \left\{ \sum_{m_n=1}^{M_n} a_{m_n} e^{j\frac{2\pi}{\lambda} [d_{pq, m_n}(t) - d_{\tilde{p}\tilde{q}, m_n}(t - \Delta t)]} \right\} \quad (44)$$

where a_{m_n} is the amplitude expressed by $a_{m_n} = [P_{pq, m_n}(t) P_{\tilde{p}\tilde{q}, m_n}(t - \Delta t)]^{(1/2)}$, and $P_s(t, \Delta t, \Delta d)$ is the joint probability that the cluster can survive from t to $t + \Delta t$ and antenna spacing Δd .

E. RMS Doppler Spread and Delay Spread

The movements of UAV, GS, and scatterers will cause the shift of the carrier frequency. The frequency shift of the m th ray in n th path can be calculated w.r.t the derivative of propagation distance

$$v_{pq, m_n}(t) = \frac{1}{\lambda} \frac{d \left[D_{p, m_n}^T(t) + D_{q, m_n}^R(t) \right]}{dt}. \quad (45)$$

Then the Doppler power spectrum density (PSD) can be obtained by

$$S_{pq}(t, f_D) = \sum_{n=1}^{N_{pq}(t)} \sum_{m_n=1}^{M_n} P_{pq, m_n}(t) \delta(f_D - v_{pq, m_n}(t)) \quad (46)$$

where f_D is the Doppler frequency. Meanwhile, the RMS Doppler spread and RMS DS are introduced to characterize the dispersion of signal in Doppler frequency and time delay domain. The calculation of the RMS spread is the same as the calculation of the second central moment. For example, the RMS Doppler spread σ_v can be obtained by

$$\sigma_v = \sqrt{\overline{v^2} - \bar{v}^2} \quad (47)$$

where

$$\overline{v^2} = \sum_{n=1}^{N_{pq}(t)} \sum_{m_n=1}^{M_n} P_{pq, m_n}(t) v_{pq, m_n}^2 \quad (48)$$

$$\bar{v} = \sum_{n=1}^{N_{pq}(t)} \sum_{m_n=1}^{M_n} P_{pq, m_n}(t) v_{pq, m_n}. \quad (49)$$

Meanwhile, the RMS Doppler spread σ_τ can be calculated by replacing the Doppler frequency part v_{pq, m_n} by time delay part τ_{pq, m_n} in (47)–(49).

IV. RESULTS AND ANALYSIS

In the simulation, since the proposed channel model mainly focuses on small-scale fading, to clearly reveal the change rule of small-scale fading, we assume that the CIRs are normalized, i.e., the path loss is set to one. Besides, omnidirectional antennas are used and only vertical polarization is considered in the simulation. The time-variant PDPs of different trajectory settings are shown in Figs. 4 and 5. For linear trajectory in Fig. 4(a), initial UAV velocity $v_{\text{UAV}}(0) = 1$ m/s, acceleration $a_{\text{UAV}} = 0.1$ m/s². Since we intend to focus on the effect caused by the UAV movement, the velocities of scatterers and GS are set to zero. For circle trajectory in Fig. 5(a), UAV linear velocity $v_{\text{UAV}} = 3$ m/s. Both the temporal and spatial sampling results are presented in Figs. 4(a) and 5(a). For clarity, we implement downsample in figure and it can be found that using spatial sampling, equidistant sampling is realized for both constant speed and variable speed. The simulation frequencies are set to typical bands used in current and future cellular networks. In Figs. 4(b) and 5(b), the drifting of cluster parameters (power, delay), and the phenomenon of cluster birth and death can be observed. Different trends of PDP changing accord with movement characteristics of circle and linear trajectories, which presents the ability of the proposed model to simulate the arbitrary 3-D UAV trajectory.

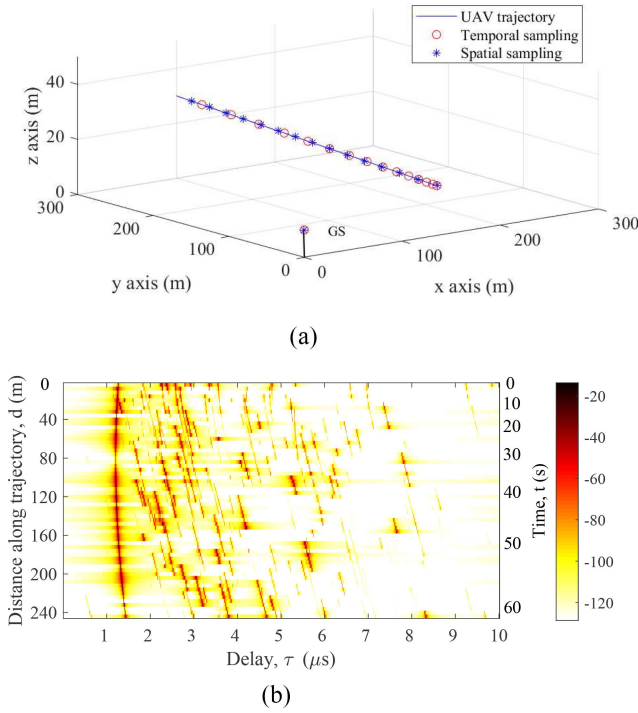


Fig. 4. Time-variant PDPs of the proposed UAV-to-ground channel model with the linear accelerated trajectory ($f_c = 2.5$ GHz, $v_g = v_c = 0$ m/s, $\lambda_G = 20$, $\lambda_R = 1$, $D_c^S = 20$ m, $f_T = 100$ Hz, $f_S = 40$ m⁻¹). (a) Accelerated linear trajectory. (b) PDPs of linear trajectory.

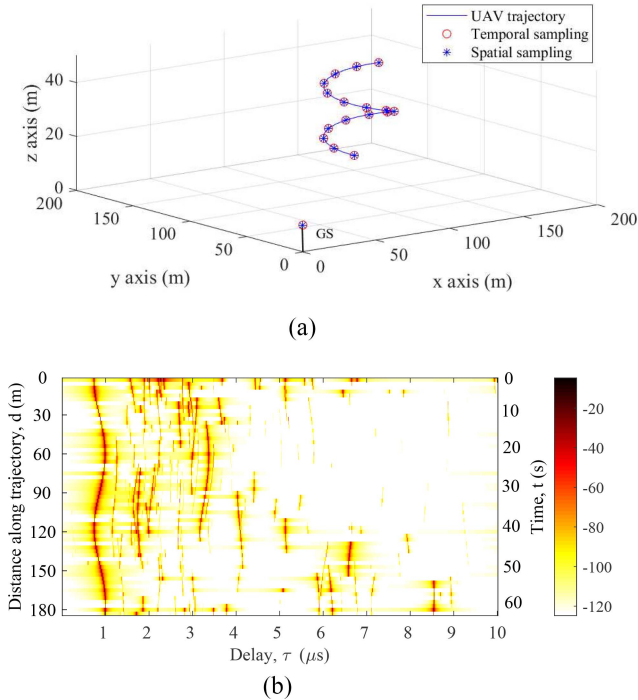


Fig. 5. Time-variant PDPs of the proposed UAV-to-ground channel model with the constant speed circle trajectory ($f_c = 2.5$ GHz, $v_g = v_c = 0$ m/s, $\lambda_G = 20$, $\lambda_R = 1$, $D_c^S = 20$ m, $f_T = 100$ Hz, $f_S = 40$ m⁻¹). (a) Constant speed circle trajectory. (b) PDPs of circle trajectory.

The absolute values of the local temporal ACF and spatial CCF can be obtained by the simplification of local STCF by setting $\Delta d = \{0, 0\}$ or $\Delta t = 0$. Fig. 6 gives the variations of temporal ACF w.r.t. carrier frequencies and time. The UAV

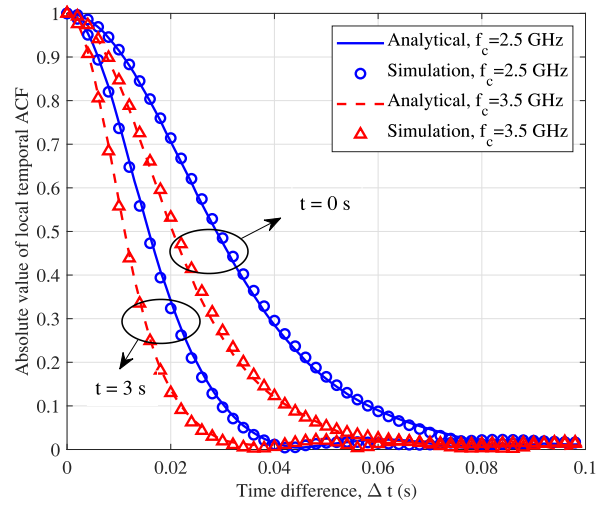


Fig. 6. Temporal ACFs with different frequencies and time instants ($v_A = v_Z = 0.1$ m/s, initial UAV velocity $v_{UAV}(0) = 3$ m/s, acceleration $a_{UAV} = 1$ m/s², $\lambda_G = 20$, $\lambda_R = 1$).

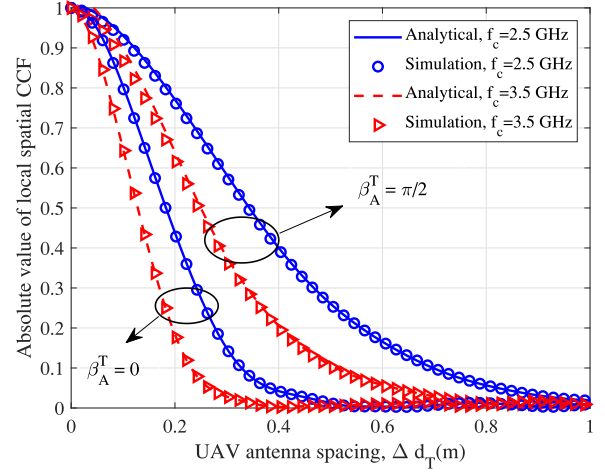


Fig. 7. Spatial CCFs with different frequencies and antenna orientations ($D_c^S = 20$ m, $\psi_{A,n}^T = 0$, $\psi_{E,n}^T = \pi/6$, $\beta_E^T = \pi/6$, $\sigma_n = 20$).

trajectory is set as linear acceleration. With the increase of UAV velocity, the decline of temporal correlation becomes faster, which indicates that increasing of UAV velocity will cause more dramatical channel variation. Besides, the impacts of different frequencies on the temporal correlations of the channel model can be observed. Higher carrier frequency will induce larger phase shift, which will reduce the temporal correlation. In our simulation, the analytical results are calculated according to derivation of STCF, and the simulation results are obtained by correlation of CIR at different time instants. The consistency between the analytical results and simulated results ensures the correctness of our simulations and derivations.

Fig. 7 represents the variations of spatial CCF according to carrier frequencies and directions of the UAV antenna array. When the UAV antenna array point to the main distribution direction of scatterers and use the higher carrier frequency, the lower spatial correlation can be achieved. Meanwhile, simulation results are compared with analytical results to ensure the correctness of our simulations and derivations.

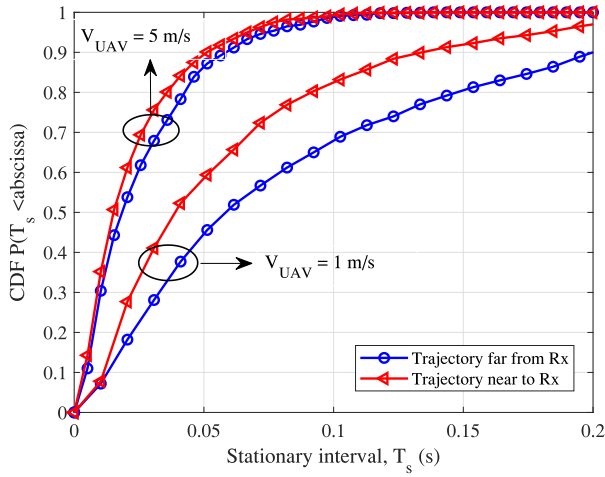


Fig. 8. CDF of stationary interval with different trajectories ($f_c = 2.5$ GHz, initial UAV velocity, acceleration $a_{UAV} = 0$ m/s², $v_g = v_c = 0$ m/s, $\lambda_G = 20$, $\lambda_R = 1$, $D_c^S = 20$ m, $\psi_{A,n}^T = 0$, $\psi_{E,n}^T = \pi/6$, $\beta_E^T = \pi/6$).

Fig. 8 shows the cumulative distribution function (CDF) of the stationary intervals with different UAV flying velocities and trajectories. The scattering mode is set as single bounce to simulate the open scenario. The vertical distance from GS to trajectory near to GS is 50 m, and the vertical distance from GS to trajectory far from GS is 100 m. Clearly, we can observe that higher UAV moving velocity will reduce the stationary interval of UAV-to-ground channels. Something worth mentioning is that when UAV goes through GS with linear trajectory, if the trajectory is close to GS, the stationary interval will be smaller than the trajectory far from GS. That may be because when UAV flies near the GS, the angular parameters will change more dramatically, making the UAV-to-ground channel fluctuates more frequently.

Fig. 9 provides the fitting result of RMS Doppler spread with the channel measurement data at the residential area. The measurement field is a neighborhood with relative flat terrain located in Chandler, AZ, USA, and the measurement frequency is 5.8 GHz [41]. The model parameters are obtained by the minimum mean square error (MMSE) fitting criterion, i.e., $\varepsilon = |\hat{F} - F(\mathcal{P})|^2$, where \hat{F} and F are the measurement and derived statistical properties, and \mathcal{P} is the fitted parameter set. It can be observed that the proposed model can fit well with the measurement data, which verifies that the proposed model can capture channel power spread features in Doppler frequency domain. Both analytical and simulation results are offered to illustrate the consistency of derivation and calculation.

Fig. 10 gives the fitting results of coherence bandwidth with measurement data. The measurement was conducted at the open field and the ultrawideband (UWB) technique was applied. The measurement frequency is from 3.1 GHz to 5.3 GHz with an operation center frequency of 4.3 GHz [42]. From the fitting results, we can see that the coherence bandwidth variation trend of the proposed model is the same as measurement results, i.e., at the higher altitude, the UAV-to-ground channels tend to have the lower coherence bandwidth. The fitting result shows that the variation trend of coherence bandwidth at different altitudes is consistent

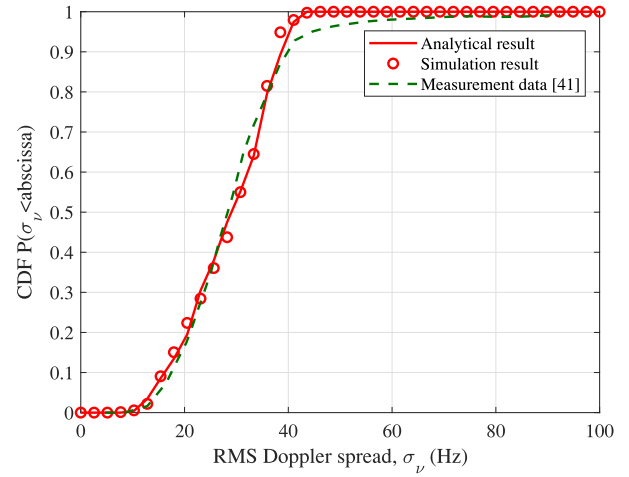


Fig. 9. CDF of RMS Doppler spread ($f_c = 5.8$ GHz, $v_c = v_g = 0$ m/s, $\lambda_G = 20$, $\lambda_R = 1$, $D_c^S = 20$ m, $\sigma_n = 20$).

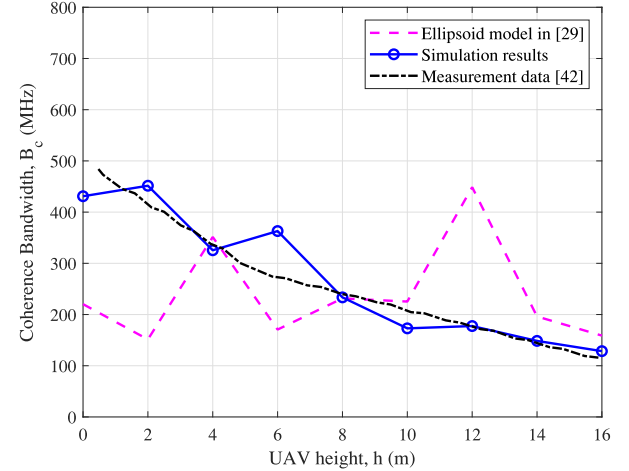


Fig. 10. Coherence bandwidth (measurement UWB from 3.1 GHz to 5.3 GHz, UAV altitude from 0 m to 18 m, $v_c = v_g = 0$ m/s, $\lambda_G = 20$, $\lambda_R = 1$, $D_c^S = 20$ m, $\Delta h = 2$ m).

with realistic scenarios. Besides, an ellipsoid UAV-to-ground GBSM is used for comparison. Since height specific LSPs are not taken into account, ellipsoid model in [29] cannot mimic changing of coherence bandwidth w.r.t. UAV heights. Meanwhile, the ellipsoid model assumes that MPCs in the same cluster distribute on an ellipsoid and have same delays, which reduces the delay resolution. Therefore, the estimation of coherence bandwidth using the ellipsoid model has larger variance. The validation results illustrate that our model has ability to simulate wideband channel characteristics. Greater bandwidth means higher time delay resolution [43]. The proposed model considers different time delays of different rays in the same cluster, which will increase time delay resolution.

Fig. 11 compares the RMS DSs with the proposed model at different flying periods. The simulation trajectory is a ascending trajectory with constant speed. In time period 0–10 s, UAV flies in low altitude below 30 m. Then in time period 10–20 s, UAV flies in high altitude above 30 m. The simulation results are compared with another measurement data obtained from

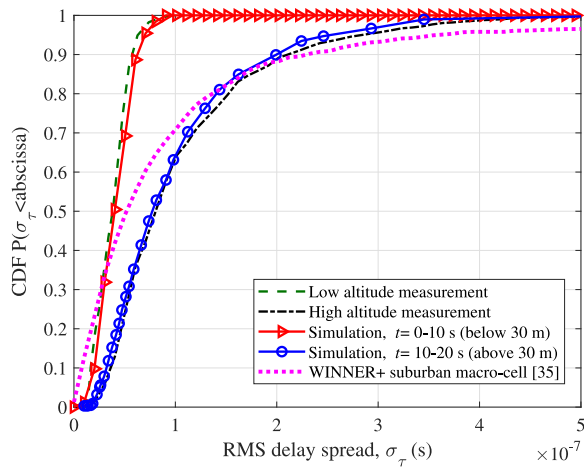


Fig. 11. CDF of RMS DS ($f_c = 2.58$ GHz, $v_c = v_g = 0$ m/s, $\lambda_G = 20$, $\lambda_R = 1$, $D_c^S = 20$ m, $h_t = 60$ m, $h_b = 10$ m).

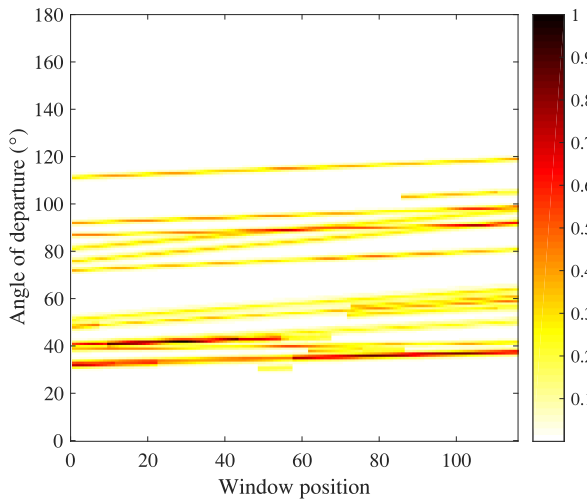


Fig. 12. Angle power spectrum at the Tx side ($f_c = 2.5$ GHz, $\lambda_G = 20$, $\lambda_R = 1$, $D_c^A = 100$ m).

the suburban scenario UAV to BS channel measurement [14]. The sounding frequency is 2.58 GHz which is used in the current cellular networks. The variation of RMS DS fits well with measurement results in both high altitude and low altitude, which validates that the proposed model can mimic channel power spread in time delay domain at different altitudes and support changing of statistical properties in long time channel simulation. Besides, the simulation result from terrestrial channel model WINNER+ [35] is provided for reference. It can be observed that RMS DS of the UAV-to-ground channel has lower variance.

The angle power spectrum of the proposed channel model at the Tx side is presented in Fig. 12. A window consisting of 12 consecutive antennas is slid along the array in order to capture the nonstationary properties of the channel on the array axis. Cluster birth-death, angular drifting, and smooth power variations of cluster power can be observed.

V. CONCLUSION

In this article, we have proposed a 3-D nonstationary UAV-to-ground GBSM for UAV integrated 6G wireless networks. The proposed model is able to characterize the UAV-to-ground

channel with arbitrary 3-D UAV trajectory changes and supports long time dynamic channel simulations at different UAV altitudes. The cluster evolution mechanisms, including the birth-death process and drifting SSPs, have been introduced to represent the scenario changes w.r.t. UAV trajectories and antenna spacing. Based on the proposed model, important channel characteristics, such as PDP, stationary interval, STCF, Doppler PSD, RMS DS, and RMS Doppler spread, have been derived and analyzed. The simulation results can fit the analytical results well, showing the correctness of both derivations and parameter generation methods in simulations. Furthermore, the RMS DS, RMS Doppler spread, and coherence bandwidth of the proposed channel model have been verified by channel measurement results.

Benefiting from high temporal and spatial resolutions, the proposed channel model framework can support mmWave and massive MIMO channel simulations by interpolating suitable UAV-to-ground channel parameter sets. Our future works include investigation of UAV-to-UAV channels with multiple mobilities and UAV communication system performance evaluation and optimization based on the proposed channel models.

REFERENCES

- [1] Y. Zeng, R. Zhang, and T. J. Lim, "Wireless communications with unmanned aerial vehicles: Opportunities and challenges," *IEEE Commun. Mag.*, vol. 54, no. 5, pp. 36–42, May 2016.
- [2] "Study on enhanced LTE support for aerial vehicles (release 15), v15.0.0," 3GPP, Sophia Antipolis, France, Rep. TR 36.777, Dec. 2017.
- [3] S. Hayat, E. Yanmaz, and R. Muzaffar, "Survey on unmanned aerial vehicle networks for civil applications: A communications viewpoint," *IEEE Commun. Surveys Tuts.*, vol. 18, no. 4, pp. 2624–2661, 4th Quart., 2016.
- [4] Z. Zhang *et al.*, "6G wireless networks: Vision, requirements, architecture, and key technologies," *IEEE Veh. Technol. Mag.*, vol. 14, no. 3, pp. 28–41, Sep. 2019.
- [5] M. Mozaffari, W. Saad, M. Bennis, Y. Nam, and M. Debbah, "A tutorial on UAVs for wireless networks: Applications, challenges, and open problems," *IEEE Commun. Surveys Tuts.*, vol. 21, no. 3, pp. 2334–2360, 3rd Quart., 2019.
- [6] B. Li, Z. Fei, and Y. Zhang, "UAV communications for 5G and beyond: Recent advances and future trends," *IEEE Int. Things J.*, vol. 6, no. 2, pp. 2241–2263, Apr. 2019.
- [7] C.-X. Wang, J. Huang, H. Wang, X. Gao, X.-H. You, and Y. Hao, "6G oriented wireless communication channel characteristics analysis and modeling," *Chin. J. Int. Things*, vol. 4, no. 1, pp. 19–32, Mar. 2020.
- [8] C.-X. Wang, J. Bian, J. Sun, W. Zhang, and M. Zhang, "A survey of 5G channel measurements and models," *IEEE Commun. Surveys Tuts.*, vol. 20, no. 4, pp. 3142–3168, 4th Quart., 2018.
- [9] K. Takizawa, T. Kagawa, S. Lin, F. Ono, H. Tsuji, and R. Miura, "C-band aircraft-to-ground (A2G) radio channel measurement for unmanned aircraft systems," in *Proc. WPMC*, Sydney, NSW, Australia, Jun. 2014, pp. 754–758.
- [10] D. W. Matolak and R. Sun, "Unmanned aircraft systems: Air-ground channel characterization for future applications," *IEEE Trans. Veh. Technol.*, vol. 10, no. 2, pp. 79–85, Jun. 2015.
- [11] D. W. Matolak and R. Sun, "Air-ground channel characterization for unmanned aircraft systems—Part I: Methods, measurements, and models for over-water settings," *IEEE Trans. Veh. Technol.*, vol. 66, no. 1, pp. 26–44, Jan. 2017.
- [12] R. Sun and D. W. Matolak, "Air-ground channel characterization for unmanned aircraft systems Part II: Hilly and mountainous settings," *IEEE Trans. Veh. Technol.*, vol. 66, no. 3, pp. 1913–1925, Mar. 2017.
- [13] M. Simunek, F. P. Fontan, P. Pechac, and F. J. D. Otero, "Space diversity gain in urban area low elevation links for surveillance applications," *IEEE Trans. Antennas Propag.*, vol. 61, no. 12, pp. 6255–6260, Dec. 2013.
- [14] X. Cai *et al.*, "An empirical air-to-ground channel model based on passive measurements in LTE," *IEEE Trans. Veh. Technol.*, vol. 68, no. 2, pp. 1140–1154, Feb. 2019.

- [15] Q. Feng, J. McGeehan, E. K. Tameh, and A. R. Nix, "Path loss models for air-to-ground radio channels in urban environments," in *Proc. VTC*, Melbourne, VIC, Australia, Jun. 2006, pp. 2901–2905.
- [16] W. Khawaja, O. Ozdemir, and I. Guvenc, "UAV air-to-ground channel characterization for mmWave systems," in *Proc. VTC-Fall*, Toronto, ON, Canada, Aug. 2017, pp. 1–5.
- [17] W. Khawaja, I. Guvenc, D. W. Matolak, U. Fiebig, and N. Schneckenburger, "A survey of air-to-ground propagation channel modeling for unmanned aerial vehicles," *IEEE Commun. Surveys Tuts.*, vol. 21, no. 3, pp. 2361–2391, 3rd Quart., 2019.
- [18] Q. Zhu *et al.*, "A novel 3D non-stationary vehicle-to-vehicle channel model and its spatial-temporal correlation properties," *IEEE Access*, vol. 6, pp. 43633–43643, 2018.
- [19] J. Bian *et al.*, "A 3D wideband non-stationary multi-mobility model for vehicle-to-vehicle MIMO channels," *IEEE Access*, vol. 7, pp. 32562–32577, 2019.
- [20] A. Ghazal *et al.*, "A non-stationary IMT-A MIMO channel model for high-mobility wireless communication systems," *IEEE Trans. Wireless Commun.*, vol. 16, no. 4, pp. 2057–2068, Apr. 2017.
- [21] Y. Liu, C.-X. Wang, J. Huang, J. Sun, and W. Zhang, "Novel 3-D non-stationary mmWave massive MIMO channel models for 5G high-speed train wireless communications," *IEEE Trans. Veh. Technol.*, vol. 68, no. 3, pp. 2077–2086, Mar. 2019.
- [22] Y. Liu, C.-X. Wang, C. F. Lopez, G. Goussetis, Y. Yang, and G. K. Karagiannidis, "3D non-stationary wideband tunnel channel models for 5G high-speed train wireless communications," *IEEE Trans. Intell. Transp. Syst.*, vol. 21, no. 1, pp. 259–272, Jan. 2020.
- [23] Y. Liu, A. Ghazal, C.-X. Wang, X. Ge, Y. Yang, and Y. Zhang, "Channel measurements and models for high-speed train wireless communication systems in tunnel scenarios: A survey," *Sci. China Inf. Sci.*, vol. 60, no. 8, pp. 1–17, Oct. 2017.
- [24] Y. Liu, C.-X. Wang, C. F. Lopez, and X. Ge, "3D non-stationary wideband circular tunnel channel models for high-speed train wireless communication systems," *Sci. China Inf. Sci.*, vol. 60, no. 8, pp. 1–13, Aug. 2017.
- [25] C.-X. Wang, A. Ghazal, B. Ai, P. Fan, and Y. Liu, "Channel measurements and models for high-speed train communication systems: A survey," *IEEE Commun. Surveys Tuts.*, vol. 18, no. 2, pp. 974–987, 2nd Quart., 2016.
- [26] L. Zeng, X. Cheng, C.-X. Wang, and X. Yin, "A 3D geometry-based stochastic channel model for UAV-MIMO channels," in *Proc. WCNC*, San Francisco, CA, USA, Sep. 2017, pp. 1–5.
- [27] Y. Li and X. Cheng, "New deterministic and statistical simulation models for non-isotropic UAV-MIMO channels," in *Proc. WCSP*, Nanjing, China, Sep. 2017, pp. 1–6.
- [28] L. Zeng, X. Cheng, C.-X. Wang, and X. Yin, "Second order statistics of non-isotropic UAV Ricean fading channels," in *Proc. IEEE VTC-Fall*, Toronto, ON, Canada, Sep. 2017, pp. 1–5.
- [29] H. Chang, J. Bian, C.-X. Wang, Z. Bai, W. Zhou, and E. M. Aggoune, "A 3D non-stationary wideband GBMS for low-altitude UAV-to-ground V2V MIMO channels," *IEEE Access*, vol. 7, pp. 70719–70732, 2019.
- [30] H. Jiang, Z. Zhang, and G. Gui, "Three-dimensional non-stationary wideband geometry-based UAV channel model for A2G communication environments," *IEEE Access*, vol. 7, pp. 26116–26122, 2019.
- [31] S. Jaeckel, L. Raschkowski, L. Thiele, F. Burkhardt, and E. Everlein, *QuaDRiGa-Quasi Deterministic Radio Channel Generator, User Manual and Documentation, V2.2.0*, Fraunhofer Herinrich Hertz Institute, Berlin, Germany, 2019.
- [32] *Study on Channel Model for Frequencies From 0.5 to 100 GHz (Release 14)*, V14.0.0, 3GPP, Sophia Antipolis, France, Rep. TR 38.901, Mar. 2017.
- [33] *5G Channel Model for Bands up to 100 GHz, V2.0*, Aalto University, Espoo, Finland, Mar. 2014.
- [34] S. Ju and T. S. Rappaport, "Simulating motion - incorporating spatial consistency into NYUSIM channel model," in *Proc. IEEE VTC-Fall*, Chicago, IL, USA, Aug. 2018, pp. 1–6.
- [35] J. Meimila, P. Kyösti, L. Henttilä, T. Jamsa, E. K. E. Suikkanen, and M. Narandzia, "WINNER+ final channel models," document CELTIC/CP5-026 D5.3, Celtic, Glasgow, Scotland, Jun. 2010.
- [36] K. I. Pedersen, P. E. Mogensen, and B. H. Fleury, "A stochastic model of the temporal and azimuthal dispersion seen at the base station in outdoor propagation environments," *IEEE Trans. Veh. Technol.*, vol. 49, no. 2, pp. 437–447, Mar. 2000.
- [37] K. Mammis, P. Santi, and A. Goulios, "A three-dimensional angular scattering response including path powers," *IEEE Trans. Wireless Commun.*, vol. 11, no. 4, pp. 1321–1333, Apr. 2012.
- [38] J. Bian *et al.*, "A WINNER+ based 3-D non-stationary wideband MIMO channel model," *IEEE Trans. Wireless Commun.*, vol. 17, no. 3, pp. 1755–1767, Mar. 2018.
- [39] C. Chen, Z. Zhong, and B. Ai, "Stationarity intervals of time-variant channel in high speed railway scenario," *China Commun.*, vol. 9, no. 8, pp. 64–70, Aug. 2012.
- [40] S. Wu, C.-X. Wang, E. H. M. Aggoune, M. M. Alwakeel, and X. H. You, "A general 3D non-stationary 5G wireless channel model," *IEEE Trans. Commun.*, vol. 66, no. 7, pp. 3065–3078, Jul. 2018.
- [41] R. M. Gutierrez, H. Yu, Y. Rong, and D. W. Bliss, "Time and frequency dispersion characteristics of the UAS wireless channel in residential and mountainous desert terrains," in *Proc. CCNC*, Las Vegas, NV, USA, Jun. 2017, pp. 516–521.
- [42] W. Khawaja, I. Guvenc, and D. Matolak, "UWB channel sounding and modeling for UAV air-to-ground propagation channels," in *Proc. IEEE Globecom*, Washington, DC, USA, Dec. 2016, pp. 1–7.
- [43] J. Huang, C.-X. Wang, Y. Liu, J. Sun, and W. Zhang, "A novel 3D GBMS for mmWave MIMO channels," *Sci. China Inf. Sci.*, vol. 61, no. 10, pp. 1–15, Oct. 2018.



Hengtai Chang received the B.Sc. degree from the School of Information Science and Engineering, Shandong University, Qingdao, China, in 2016, where he is currently pursuing the Ph.D. degree.

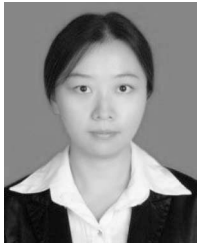
His current research interests include UAV communications, wireless propagation channel measurements and channel modeling, and B5G/6G wireless communications.



Cheng-Xiang Wang (Fellow, IEEE) received the B.Sc. and M.Eng. degrees in communication and information systems from Shandong University, Qingdao, China, in 1997 and 2000, respectively, and the Ph.D. degree in wireless communications from Aalborg University, Aalborg, Denmark, in 2004.

He was a Research Assistant with the Hamburg University of Technology, Hamburg, Germany, from 2000 to 2001, a Visiting Researcher with Siemens AG Mobile Phones, Munich, Germany, in 2004, and a Research Fellow with the University of Agder, Grimstad, Norway, from 2001 to 2005. He has been with Heriot-Watt University, Edinburgh, U.K., since 2005, where he was promoted to a Professor in 2011. In 2018, he joined Southeast University, Nanjing, China, as a Professor. He is also a part-time Professor with Purple Mountain Laboratories, Nanjing. He has authored four books, two book chapters, and about 400 papers in refereed journals and conference proceedings, including 24 ESI Highly Cited Papers. He has also delivered 20 Invited Keynote Speeches/Talks and seven tutorials in international conferences. His current research interests include wireless channel measurements and modeling, B5G wireless communication networks, and applying artificial intelligence to wireless communication networks.

Prof. Wang received eleven Best Paper Awards from IEEE GLOBECOM 2010, IEEE ICCT 2011, ITST 2012, IEEE VTC 2013-Spring, IWCMC 2015, IWCMC 2016, IEEE/CIC ICC 2016, WPMC 2016, WOCC 2019, and IWCMC 2020 and a Highly-Cited Researcher recognized by Clarivate Analytics from 2017 to 2019. He is currently an Executive Editorial Committee Member of the IEEE TRANSACTIONS ON WIRELESS COMMUNICATIONS. He has served as an Editor for nine international journals, including the IEEE TRANSACTIONS ON WIRELESS COMMUNICATIONS from 2007 to 2009, the IEEE TRANSACTIONS ON VEHICULAR TECHNOLOGY from 2011 to 2017, and the IEEE TRANSACTIONS ON COMMUNICATIONS from 2015 to 2017. He was a Guest Editor of the IEEE JOURNAL ON SELECTED AREAS IN COMMUNICATIONS, Special Issue on Vehicular Communications and Networks (Lead Guest Editor), Special Issue on Spectrum and Energy Efficient Design of Wireless Communication Networks, and Special Issue on Airborne Communication Networks. He was also a Guest Editor of the IEEE TRANSACTIONS ON BIG DATA, Special Issue on Wireless Big Data, and he is a Guest Editor of the IEEE TRANSACTIONS ON COGNITIVE COMMUNICATIONS AND NETWORKING, Special Issue on Intelligent Resource Management for 5G and Beyond. He has served as a TPC Member, the TPC Chair, and the General Chair for over 80 international conferences. He is a member of the Academia Europaea, a Fellow of the IET, and an IEEE Communications Society Distinguished Lecturer in 2019 and 2020.



Yu Liu received the Ph.D. degree in communication and information systems from Shandong University, Jinan, China, in 2017.

From 2015 to 2017, she was a Visiting Scholar with the School of Engineering and Physical Sciences, Heriot-Watt University, Edinburgh, U.K. From 2017 to 2019, she was a Postdoctoral Research Associate with the School of Information Science and Engineering, Shandong University, where she has been an Associate Professor with the School of Microelectronics since 2019. Her main research

interests include nonstationary wireless MIMO channel modeling, high-speed train wireless propagation characterization and modeling, and channel modeling for special scenarios.



Wensheng Zhang (Member, IEEE) received the M.E. degree in electrical engineering from Shandong University, Qingdao, China, in 2005, and the Ph.D. degree in electrical engineering from Keio University, Tokyo, Japan, in 2011.

In 2011, he joined the School of Information Science and Engineering, Shandong University, where he is currently an Associate Professor. He was a Visiting Scholar with the University of Oulu, Oulu, Finland, in 2010 and the University of Arkansas, Fayetteville, AR, USA, 2019. His research interests

lie in tensor computing, random matrix theory, and intelligent B5G wireless communications.

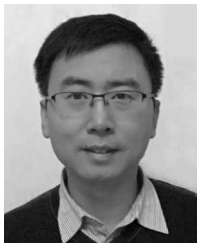


Jie Huang (Member, IEEE) received the B.E. degree in information engineering from Xidian University, Xi'an, China, in 2013, and the Ph.D. degree in communication and information systems from Shandong University, Qingdao, China, in 2018.

From January 2019 to February 2020, he was a Postdoctoral Research Associate with Durham University, Durham, U.K. He is currently a Postdoctoral Research Associate with the National Mobile Communications Research Laboratory, Southeast University, Nanjing, China,

and also a Researcher with Purple Mountain Laboratories, Nanjing. His research interests include millimeter wave and massive MIMO channel measurements and channel modeling, intelligent reflecting surface, wireless big data, and B5G/6G wireless communications.

Dr. Huang received the Best Student Paper Award at WPMC'16.



Jian Sun (Member, IEEE) received the B.Sc. degree in applied electronic technology, the M.Eng. degree in measuring and testing technologies and instruments, and the Ph.D. degree in communication and information systems from Zhejiang University, Hangzhou, China, in 1996, 1999, and 2005, respectively.

From 2005 to 2018, he was a Lecturer with the School of Information Science and Engineering, Shandong University, Qingdao, China, where he has been an Associate Professor since 2018. In 2008,

he was a Visiting Scholar with the University of California at San Diego, La Jolla, CA, USA. In 2011, he was a Visiting Scholar with Heriot-Watt University, Edinburgh, U.K., supported by U.K.–China Science Bridges: R&D on B4G Wireless Mobile Communications project. His current research interests include signal processing for wireless communications, channel sounding and modeling, propagation measurement and parameter extraction, maritime communication, visible light communication, software defined radio, MIMO, multicarrier, and wireless systems design and implementation.



Xiqi Gao (Fellow, IEEE) received the Ph.D. degree in electrical engineering from Southeast University, Nanjing, China, in 1997.

In April 1992, he joined the Department of Radio Engineering, Southeast University. He has been a Professor of information systems and communications with Southeast University since May 2001. Since March 2019, he has been a part-time Professor with Purple Mountain Laboratories, Nanjing. From September 1999 to August 2000, he was a Visiting Scholar with the Massachusetts

Institute of Technology, Cambridge, MA, USA, and Boston University, Boston, MA, USA. From August 2007 to July 2008, he visited the Darmstadt University of Technology, Darmstadt, Germany, as a Humboldt Scholar. His current research interests include broadband multicarrier communications, MIMO wireless communications, channel estimation, turbo equalization, and multirate signal processing for wireless communications.

Prof. Gao received the Science and Technology Awards of the State Education Ministry of China in 1998, 2006, and 2009, the National Technological Invention Award of China in 2011, and the IEEE Communications Society Stephen O. Rice Prize Paper Award in the Field of Communications Theory in 2011. From 2007 to 2012, he served as an Editor for the IEEE TRANSACTIONS ON WIRELESS COMMUNICATIONS, the IEEE TRANSACTIONS ON SIGNAL PROCESSING from 2009 to 2013, and the IEEE TRANSACTIONS ON COMMUNICATIONS from 2015 to 2017.